Chapter 4

Controlled field evaluation on asphalt pavement test section using NDT techniques

4.1. Introduction

A structurally sound pavement undergoing premature failure is one of the major causes of concern in recent times. Delamination caused due to debonding between the asphalt layers at layer interfaces is one such phenomenon which adversely affects the pavement performance. To ensure the structural integrity of asphalt pavements or overlays, it is necessary to achieve a proper degree of bond at these interfaces. An adequate tack coat ensures that the tacked layers behave as a structural monolith against traffic loading and environmental effects. Poor construction practices, temperature stresses or high vehicular loading may be attributed to the causes of debonding. Direct assessment of in-situ debonding is difficult. Its visual detection is usually not possible unless it appears on the surface in the form of crescent-shaped slippage cracks; mostly at the locations where high horizontal stresses occur. Destructive coring is not a true representation of the entire area and thus not suitable for evaluating long lengths of pavement. It can be used only to measure the severity and depth of debonding. Debonded areas are often associated with various indicators such as longitudinal cracking in the wheel path, higher surface deflections, higher moisture content, reduced density and pavement material stiffness. Local failure in the asphalt layer may also occur due to the existence of any underground anomaly buried within or under the layers.

A number of Non-Destructive Testing (NDT) methods have been developed for accurate testing and evaluation of pavements. However, different methods provide varying levels of accuracy in investigating different aspects of pavement health. The review of literature helped to identify NDT technologies that have the potential to detect debonding and underground anomaly, including Infrared Thermography (IRT), Ground-Penetrating Radar (GPR), mechanical wave propagation methods and deflection basin methods.

The objectives of this chapter are to determine the efficacy of IRT to detect debonding and underground anomalies in asphalt pavements, estimate the field inspection time zones for Indian conditions using IRT, and assess the improvement in their detectability, if any, using application of other NDT methods. To accomplish these objectives, tests are to be strictly monitored under controlled conditions for which the in-situ facility is designed and constructed as per the details presented in Chapter 3. The findings of NDT tests conducted on the in-situ facility are presented. Based on the availability of equipment, three NDT technologies have been used in this study, namely, IRT, GPR and Light Weight Deflectometer (LWD). The suitability and performance of these technologies for network-level investigations is discussed. The chapter concludes with the summary of findings and future work that can be undertaken.

4.2. Evaluation of asphalt pavement test section using IRT method

In order to perform NDT tests, an asphalt pavement test section is constructed in BITS Pilani campus and its construction details are thoroughly explained in Chapter 3. Comprehensive testing of the pavement blocks containing different bonding and anomaly conditions is conducted. The rationale for choosing the materials was to simulate actual field conditions. The first reason for selecting these different materials was that in actual field conditions, debonding might likely occur due to the presence of a sandy or clayey type of soil (from vehicle tires), or grease from vehicles or polythene since it is easier to find such materials on the road. Secondly, since the rate of heat flow through any block would depend upon the thermal conductivity of the material induced in it, therefore, to study the influence of the bonding agent on the thermal behaviour of the pavement, materials having a significant difference in their thermal conductivity values were chosen. For example, the thermal conductivity value for bentonite slurry is 3-4 W $m^{-1}K^{-1}$which is about 15-20 times more than that of sand (0.15-0.25 W $m^{-1}K^{-1}$). It was expected that they would represent different cases of interchange time durations quite widely and efficiently. Objects to simulate anomaly conditions were selected based on the high chances of finding such pipes or plates of metals buried in real field conditions. The dimensions of all the test blocks are kept the same in this study. It should be noted that the effect of thermal boundary losses and variation in sample size or dimension of test blocks are beyond the scope of this study.

IRT technique is popular to identify internal defects in concrete structures. Unlike concrete, the asphalt mix is not homogeneous and therefore, not much success has been obtained from thermographic inspections on asphalt pavements, as seen from the literature (Heitzman et al., 2013). This study makes an attempt to check the potential application of IRT testing on asphalt pavements, the depth of detectability and to identify the suitable time durations to conduct the testing. Figure 3.2 shows the detailed drawing of the actual test section and satisfactory testing results have been obtained over blocks S-1, DW-1, G-1, PO-1, B-1, and FB. It should be noted that for bonding conditions located at greater depths of 100 and 150 mm, and subsurface anomalies (remaining all blocks), no distinguishable colour changes or significant thermal images could be obtained. Thus, they have been refrained from any further IRT testing and analysis. An illustrative schematic of the blocks used for further testing is depicted in Figure 4.1, where the bond condition no bond:1 indicates sand, partial bond indicates dust along wheel path, no bond:2 indicates grease, no bond:3 indicates polythene, and no bond:4 indicates bentonite slurry.

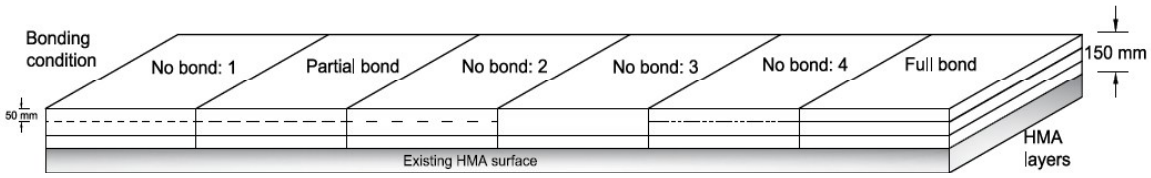

Figure 4.1. Schematic of constructed in-situ asphalt pavement test section showing different conditions of the interlayer bond

4.2.1. Instrument

The instrument used to perform thermographic inspections is called an infrared camera or thermal imaging camera or thermal imager that creates a visible colour image using infrared radiations. The images are called thermal images or thermograms and this art of capturing and analyzing thermal images is known as thermography. Being independent of the level of visible ambient light, the thermal imaging cameras work well in complete darkness which makes them very popular.

The instrument utilized for taking thermal images in this study is a FLIR T250 infrared camera (refer Figure 4.2). It consists of microbolometer as a detector whose electrical resistance is changed when infrared radiations encounter and heats it. This change of electrical resistance is measured

and converted into a range of temperatures to produce an image. Laser pointer of the camera helps to aim the target surface, and the camera collects and stores images of 320 × 240 pixels resolution. The resolution of the digital images, which were captured along with thermal images was 2048 × 1536 pixels.

Figure 4.2. FLIR T250 thermal camera

Table 4.1 summarizes some of the main technical specifications of the thermal camera (FLIR T250, 2009). It is expected that the thermal cameras with higher pixel resolution would fetch better quality thermograms and should be preferred for field applications particularly when the camera is to be mounted over a moving vehicle to take the images. Due to the unavailability of better resolution camera, this study is performed with 320 × 240 pixels resolution camera and the images of the area under study are taken closely.

Table 4.1. Technical specifications of FLIR T250 thermal camera

Particulars	Specifications	Unit
Measurement object temperature range	-20 to +350	°C
Accuracy	2% of reading or ±2	°C
Thermal sensitivity at 30°C	80	mK
Field of view	25 × 19	°
Minimum focus distance	0.4	m
Spatial resolution	2.18	mrad
Spectral range	7.5 - 13	µm

Particulars	Specifications	Unit
Imaging frequency	9	Hz
Infrared resolution	320 × 240	pixel
Digital image resolution	2048 × 1536	pixel
Focal plane array	Uncoooled microbolometer	-
Digital zoom	1–2×	-

4.2.2. Data acquisition

After procuring the thermal camera of required specifications, the important factors to be considered during the process of data acquisition are data collection time and data collection speed. In order to estimate the ideal time durations of testing, the thermal images are taken over the entire day. Since the study is limited to the test-section, the data is collected by keeping the camera stationary with the camera aperture at a height of ~0.5 meters from the pavement surface. However, for real field applications, the camera is usually mounted over a moving vehicle.

Data collection has been performed on the test section over a period of one month in order to capture the best results in accordance with ASTM standards (ASTM D4788-03, 2013). The thermograms captured for bonding conditions located at a depth of 100 mm and 150 mm, and for underground anomalies could not produce any significant colour change in the thermograms. This limits the use of thermal imaging technique to the depth of 50 mm, in this study. The images have been taken regularly over 30-minute time intervals (from 00:00 hours to 23:30 hours) and their post-processing has been performed. It is ensured that the images are captured from the same height, direction and measurement angle every time, to ensure reproducibility in measurements. Images for all the bonding conditions have been taken block-wise. Passive approach (sunlight) has been employed to produce temperature differentials on the test-pavement section. The active approach of infrared thermography in which artificial heating of the specimen under test is performed is not a feasible option for in-field pavements. Environmental conditions such as ambient air temperature, relative humidity, pavement surface temperature, wind speed, and emissivity have also been taken into consideration. Table 4.2 presents the environmental

conditions measured at the local weather station on a typical sunny summer day of testing. Pavement temperature range has been measured by thermocouple installed on the test section.

Table 4.2. Environmental conditions at the time of testing

Ambient temperature range (°C)	Relative humidity range (%)	Wind speed (km/h)	Pavement temperature range (°C)
28-40	15-57	3-10	23.6-56.5

Figure 4.3 shows a sample variation in the profile of ambient temperature, relative humidity and pavement temperature throughout the day of testing. With an increase in ambient temperature, it can be seen that pavement temperature is increasing and relative humidity is decreasing, and vice versa. The study of temperature profiles helps to estimate the time durations over which the subsurface defect can become detectable. The greater the difference in temperature between the surface above the debonded and surrounded area, also known as the thermal contrast, the defect would be more easily detectable. Therefore, the pavement temperature and ambient temperature are among the most important parameters governing the success of thermographic inspections.

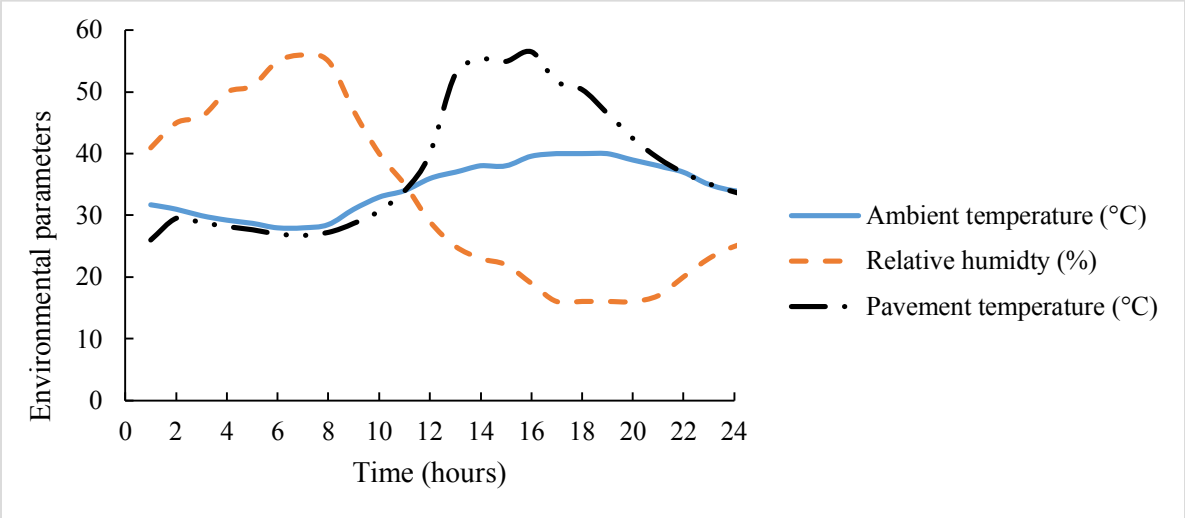

Figure 4.3. Variation in environmental parameters at the time of infrared thermography testing

4.2.3. Data processing

Visual observation of colour contrast in thermograms facilitates subjective judgment and it is more of an experience-based practice. Furthermore, under natural environmental conditions in passive thermography, many a time the colour contrast is not clearly observed. Hence, by merely looking at the thermograms, no conclusion can be obtained and often the efforts get wasted. This necessitates a more objective approach for processing of thermal images. Based on the fact that every image is a group of pixels and each of these pixels is associated with a numeric value, which can be employed mathematically, a novel methodology is developed in this study. The subsequent sections present the basics of imaging and the developed methodology.

4.2.3.1. Imaging basics

A digital image is basically a two-dimensional (2D) array of pixels, with each pixel carrying information about a small chunk of the whole image area. This 2D array, from a data-centric point of view, further divides into a three-dimensional matrix with two of the dimensions representing physical space and the third one representing different colour bands, generally three in number for a true colour image - red, green and blue. The elements of the matrix are scalars that are a measure of the intensity of the colour corresponding to the colour band they lie in, at that particular point in space. For regular 8-bit digital images, the scalars can take values from 0 to 255 ($=2^8-1$) with 0 standing for the absence of the colour and 255 standing for the colour in its maximum possible intensity. Linear interpolation between the two values translates to a linear scaling of the colour intensity. A pixel is fundamentally a one-dimensional array, with the number of elements equal to the number of colour bands in the image. It is the combination of these scalars in the pixel that determines what colour the point will look like in an image. A pixel from an 8-bit true colour image can acquire $256\times256\times256 = 16,777,216$ different combinations, meaning that it can represent those many unique colours, though only a small portion of that range is differentiable by the naked eye.

In case of a digital infrared image, the pixel represents a unique temperature value, instead of colour. Thus, in an infrared image, a pixel value is the temperature of the area that the pixel represents. And unlike colour, temperature can be represented by a single numerical value.

Therefore, the infrared images are processed on their crude grayscale versions, which are single band matrices. Infrared cameras generally capture the image and impart a colour to the temperature which aids the process of visual inspection.

4.2.3.2. Post-calibration using FLIR QuickReport Tool

The thermal images have been taken in auto mode, in order to accommodate the surface points with highest and lowest temperatures and all the other intermediate values. This ensures that there is no loss of information. It means that the 0 value was automatically set to the lowest temperature (T_l) among the temperatures of all the points in the frame and similarly, 255 to the highest (T_h). All the images have been calibrated to the same T_h and T_l values using FLIR QuickReport software (version 1.2 SP2), in order to accommodate the maximum and minimum temperature values when all of them are considered together (FLIR, 2009). Post-calibration has also been performed on the basis of the atmospheric temperature, relative humidity, acquisition height, and reflected apparent temperature of the targets. The final output of this first phase of processing was a set of 8-bit grayscale images.

4.2.3.3. Thermal image processing using MATLAB

The FLIR QuickReport output is fed as input to MATLAB and images, fundamentally being matrices, are read by MATLAB as 1200 × 1300 uint8 matrices. The uint8 suffix signifies that the matrix elements can only take integer values from 0 to 255 which is suitable only for standalone images. The various bonding conditions in the test section are uniformly spread in their respective blocks. This calls for an objective quantitative type of analysis. To see exactly how much the thermal signature of a debonded area is different from that of a bonded one, temperature histogram for each debonded condition has been plotted against the temperature histogram of the fully bonded condition, in the same MATLAB Figure. This is done to compare the distributions and enhance understanding. The grayscale pixel matrix has been converted to its corresponding temperature matrix by implementing Eq. (4.1):

$$T_{ij} = T_l + P_{ij} * \frac{(T_h - T_l)}{256} \quad (4.1)$$

where, T_{ij} is the temperature at the point corresponding to the pixel in the i^{th} row and j^{th} column, T_l is the calibrated minimum temperature, T_h is the calibrated maximum temperature, and P_{ij} is the grayscale intensity of the pixel in the i^{th} row and j^{th} column.

The histograms of these temperature matrices have then been plotted, as stated earlier. The average temperatures for the distributions have also been plotted to gauge the amount of thermal contrast.

4.2.4. Results and discussion

As per the ASTM D4788 specifications for delamination inspection on bridge decks, 'the minimum temperature difference of 0.5 °C between bonded and the debonded area is required to be detected by infrared camera, with testing performed when wind speed is less than 50 kmh^{-1}' (ASTM D4788-03, 2013). This has been observed to be true for the asphalt pavements as well. The processing in MATLAB facilitates this finding, by plotting comparative histograms between the temperature of the test section and pixel count. The average temperature line for the bonded and the debonded sections has also been shown in the plots and their corresponding thermal contrast have been calculated. This process has been repeated for all bonding conditions, at every 30-minute interval for the entire day.

Figure 4.4 presents the variation of thermal contrast for each of the debonded blocks, over a period of 24 hours. The thermal contrast can be seen to be strongly influenced by the change in ambient temperature. It is found to be increasing with an increase in ambient temperature.

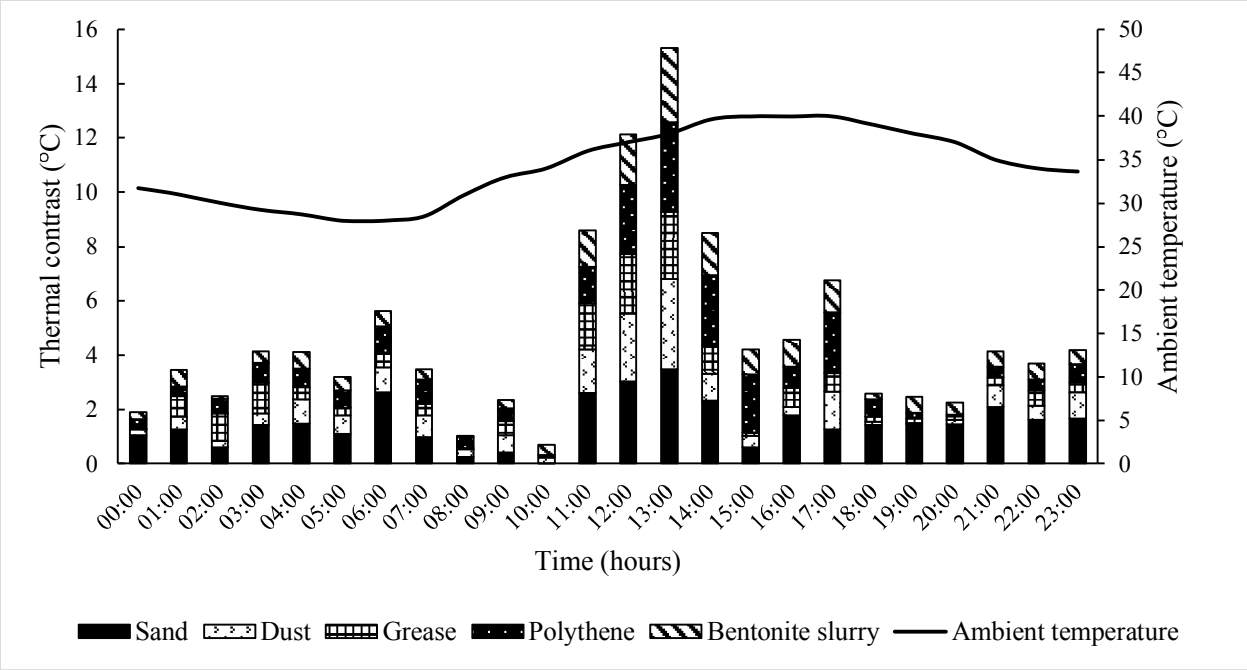

Figure 4.4. Hourly thermal contrast variation due to different interlayer bond conditions in the test section

Figures 4.5 to 4.14 present the results of thermal variation over sand debonded and fully bonded asphalt blocks. Since the best clarity results are obtained for sand debonded condition, thus, to avoid repetition and for brevity reasons, the entire process has been comprehensively explained for sand and bonded asphalt condition. Similar trends in results were obtained for all other bonding conditions also, with only difference in interchange time durations, which are presented in later sections.

Figures 4.5a and 4.5b present the raw infrared coloured and grayscale images for sand debonded and bonded asphalt conditions, respectively at around 02:30 hours. Their comparative histogram is shown in Figure 4.6. It can be seen that the temperature of the sand debonded block lies in the range of about 27.0-28.0 °C and that for the bonded block is around 28.5-29.5 °C. This is evident from the grayscale image for the bonded area as the pixels are brighter and towards higher temperature zone. Relatively, the image for the sand debonded condition is darker and lies on the lower side of the temperature scale. The thermal contrast is found to be 1.45 °C which is greater than 0.5 °C, and thus makes debonded area detectable by thermal imaging camera. This trend of bonded asphalt block being relatively warmer than the sand debonded block is observed

throughout the night. This is because of the fact that the intermediate debonded layer acts as an insulator and hinders the heat flow. It causes Hot-Mix Asphalt (HMA) block above debonding to cool or warm faster than the fully bonded asphalt block, which undergoes slow heating and cooling.

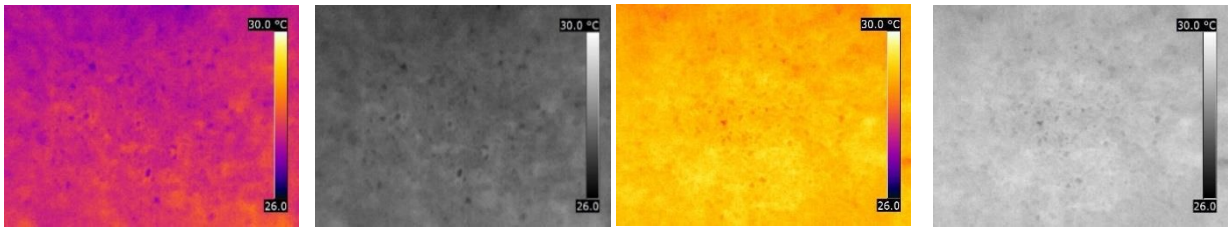

(a) Sand block **(b) Asphalt block**

Figure 4.5. Comparison of coloured and grayscale infrared images at 02:30 hours

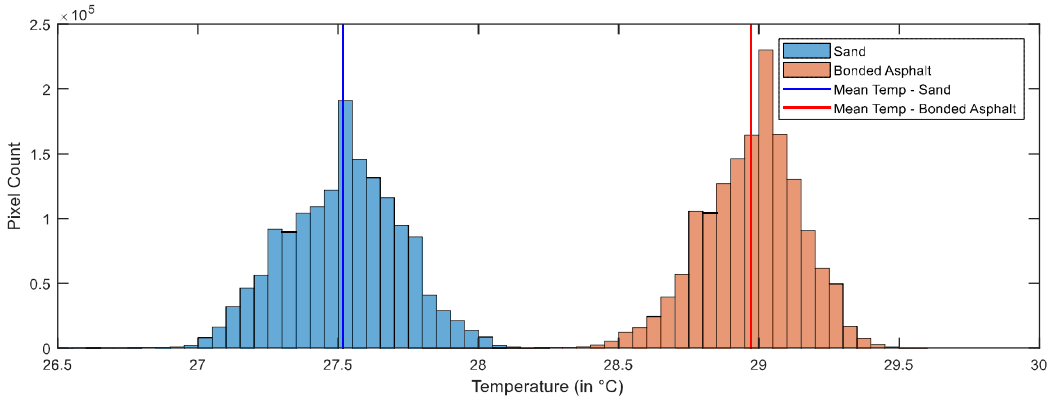

Figure 4.6. Histograms for sand and asphalt block at 02:30 hours

As the sun rises, the ambient temperature starts rising. This causes warming of the sand debonded block at a higher rate due to the presence of an internal discontinuity. It can be observed from Figures 4.7a and 4.7b that at 10:00 hours the thermal images show almost no contrast with the pixels in both being equally bright. The temperature for both sand and asphalt blocks lie in the range of about 34.5-35.5 °C. The histograms for sand and bonded asphalt, as shown in Figure 4.8 are observed to be merging during this time duration, which is an indication of similarity in thermal signatures. The thermal contrast is found to be 0.025 °C, being less than 0.5 °C. This trend is observed for around two hours in the morning (8:00 to 10:00 hours in this case). In such cases, the

debonded areas go unidentified through thermal imaging camera and infrared thermography is not found effective in detecting subsurface debonding.

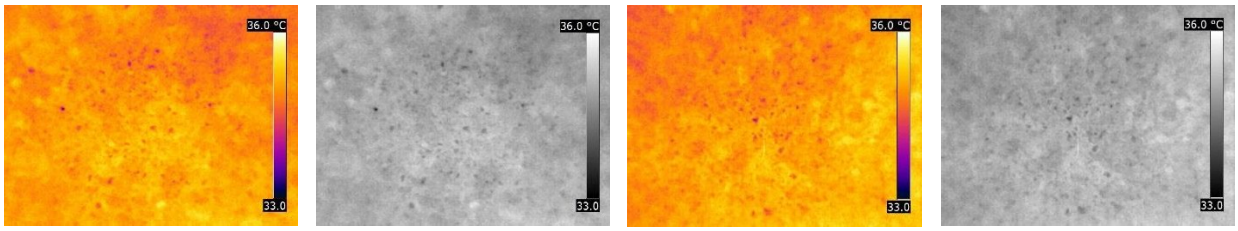

(a) Sand block **(b) Asphalt block**

Figure 4.7. Comparison of coloured and grayscale infrared images at 10:00 hours

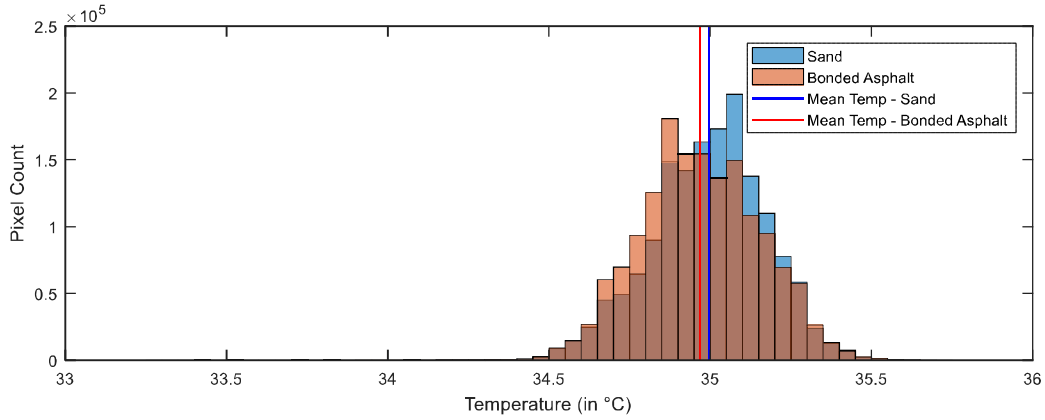

Figure 4.8. Histograms for sand and asphalt block at 10:00 hours

As the day progresses, the increasing ambient temperature and intensity of solar radiation cause sand debonded block to heat up at a higher rate than the bonded block. At around 11:00 hours, the thermal image for the sand block is brighter than that for the bonded asphalt block as seen from Figures 4.9a and 4.9b. The nature of the contrast flips, as shown in Figure 4.10. Sand debonded block lies in the temperature range of 61.5-65.8 °C, whereas bonded asphalt block lies in the temperature range of 58.5-62.5 °C. Within an hour (10:00 to 11:00 am), it is observed that the average temperature increase for the sand debonded block is around 28.8 °C whereas for bonded asphalt block is 25.5 °C. Thermal contrast is found to be around 3.2 °C, lying in the detectable range of the thermal camera.

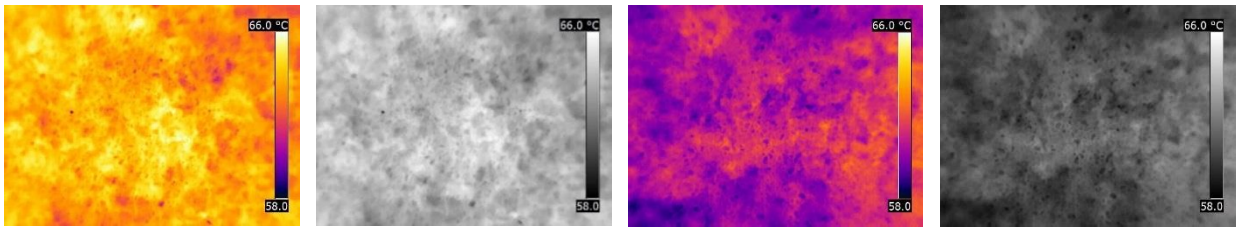

(a) Sand block **(b) Asphalt block**

Figure 4.9. Comparison of coloured and grayscale infrared images at 11:00 hours

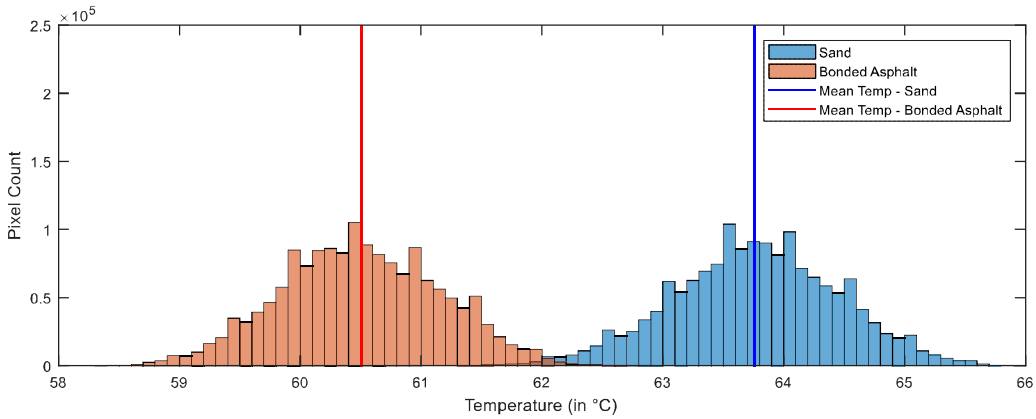

Figure 4.10. Histograms for sand and asphalt block at 11:00 hours

Further, the temperature rises for both the blocks, but rather slowly for sand block since it has almost reached its maximum possible temperature. Sand debonded block lies in the temperature range of 67.2-71.0 °C, and bonded asphalt block is around 66.5-69.5 °C. At around 15:00 hours, histograms for both of these again merge and the debonded areas again go almost indistinguishable (thermal contrast around 0.5 °C), as evident from Figures 4.11 and 4.12.

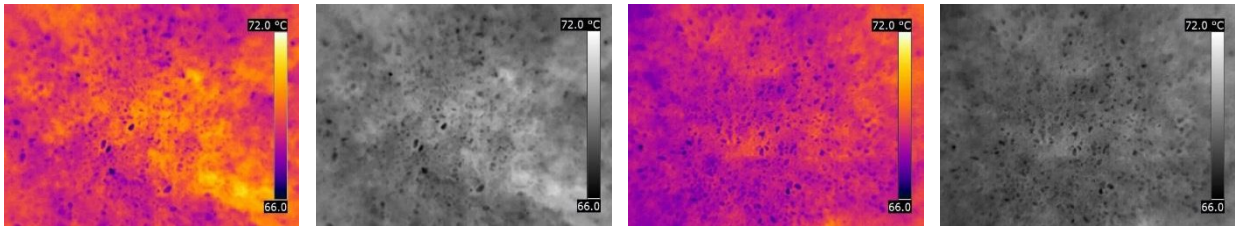

(a) Sand block **(b) Asphalt block**

Figure 4.11. Comparison of coloured and grayscale infrared images at 15:00 hours

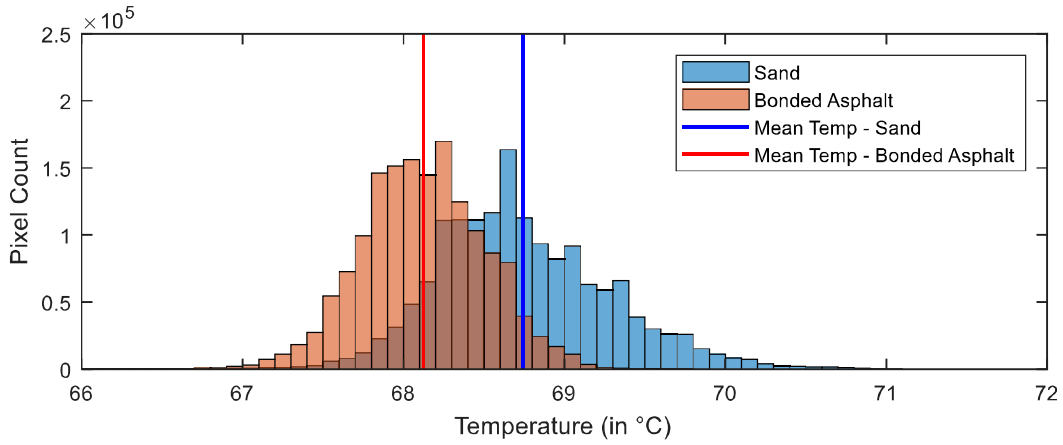

Figure 4.12. Histograms for sand and asphalt block at 15:00 hours

Sometimes, at around 17:00 hours, as observed from Figures 4.13a and 4.13b, the sand debonded block lies in temperature range of 45.5-47.7 °C whereas bonded asphalt block around 47.0-48.7 °C. Since the intensity of solar radiation reduces as the sun sets, debonded block rapidly starts cooling, whereas bonded loses heat gradually. This can be seen from darker grayscale image of sand than asphalt block and their thermal contrast is found to be 1.25 °C, lying in detectable range. The distributions again swap their positions on x-axis as seen from Figure 4.14. This trend is observed to persist throughout the evening till the end of the day.

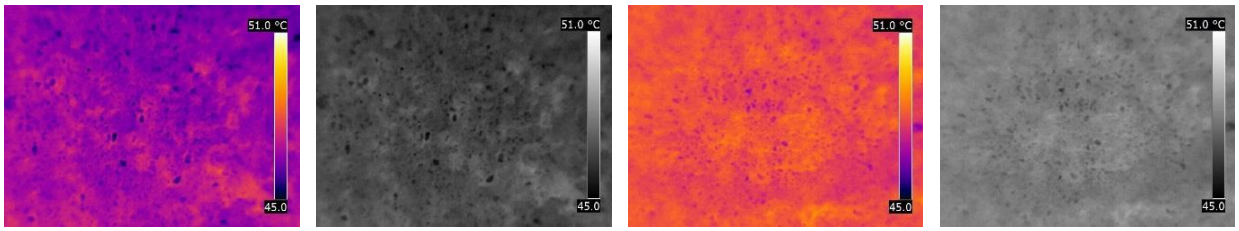

(a) Sand block **(b) Asphalt block**

Figure 4.13. Comparison of coloured and grayscale infrared images at 17:00 hours

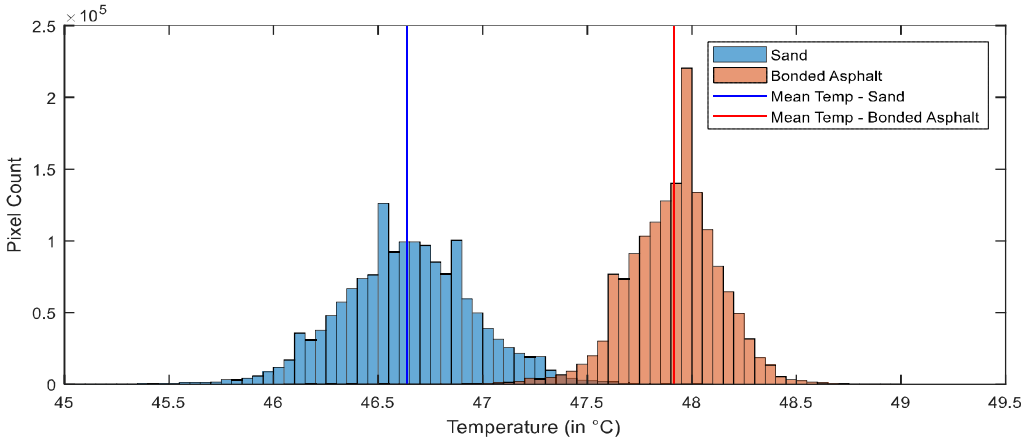

Figure 4.14. Histograms for sand and asphalt block at 17:00 hours

For this experiment under the set of mentioned conditions, the values for thermal contrast are observed to be the largest for sand debonded block, followed by dust along wheel path, polythene, bentonite slurry, and smallest for grease debonded block. The least thermal contrast values for grease can be verified by its largest interchange durations. Sand debonded block undergoes rapid thermal variation, as seen through its shortest interchange durations and largest thermal contrasts. Debonded blocks other than sand block have been observed to follow the same cyclic pattern of merging and flipping over of the histograms. However, the interchange time duration has been found to vary depending upon the thermal properties of the material used as a debonding agent. Table 4.3 summarizes this finding for all the cases. The interchange time zones for sand has been found to be 8:00 to 10:00 hours in the morning and 14:30 to 15:30 hours in the afternoon. It can thus be concluded that the time after evening to next morning is optimum to conduct a thermographic inspection of asphalt pavements since sufficient time gap is available between the two interchange durations. For other bonding conditions of partial bond, grease, polythene and bentonite slurry, the interchange time durations are found to vary largely. For grease, this duration is found to be as large as 5 hours and thermal contrast as small as 0.002 °C. Thus, the available time durations for detection of debonding caused by these agents is comparatively lesser than that of sand, and such debonding is less likely to be detected by thermal imaging camera. This proves that the agent causing debonding highly influence the defect detection based on its thermal conductivity.

Table 4.3. Summary of day heating and night cooling interchange time durations for different bond conditions

Bond condition	Interchange time durations	
	Morning (hours)	Afternoon/evening (hours)
No bond:1 (Sand)	8:00 to 10:00	14:30 to 15:30
Partial bond (Dust along wheel path)	9:30 to 10:00	17:30 to 20:00
No bond:2 (Grease)	6:30 to 10:00	18:00 to 23:00
No bond:3 (Polythene)	7:30 to 10:00	18:00 to 22:00
No bond:4 (Bentonite slurry)	7:00 to 10:00	17:30 to 20:30

Tables 4.4 to 4.7 present infrared images and histograms at few selected times for bonding conditions other than sand. The selected images for each case show the initial position of histograms representing the initial temperature difference between the blocks, the merging histograms showing the approximately same temperature of both the blocks, and the swapped position of histograms indicating the temperature reversal cycle. The colour brightness in raw infrared images can also be seen to change accordingly. Appendix-1 compiles the histograms for all the bond conditions with fully bonded asphalt, every hour of a day, and interesting results can be seen in the form of cyclic swapping of the two plots in each figure.

Table 4.4. Infrared images and histograms at different times of the day for partially bonded and bonded asphalt blocks

Time	Raw infrared image		Histogram
04:00 hours	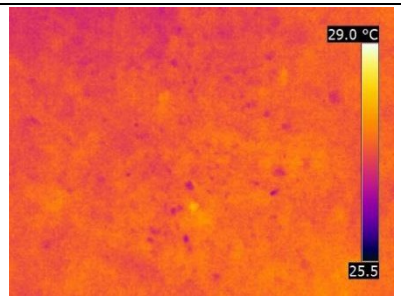	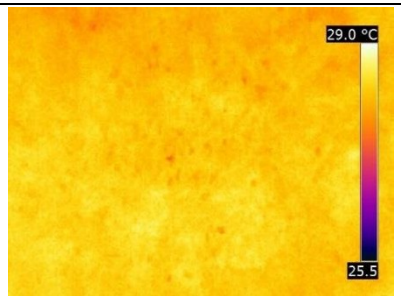	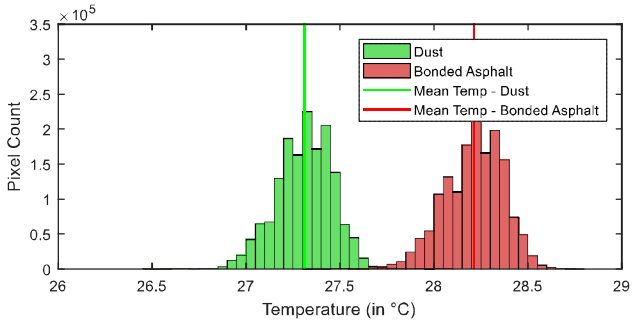
10:00 hours	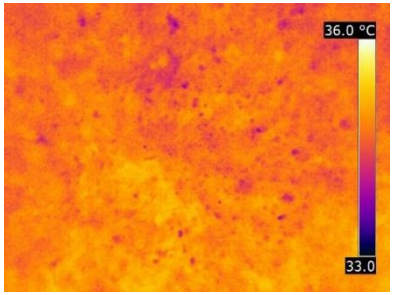	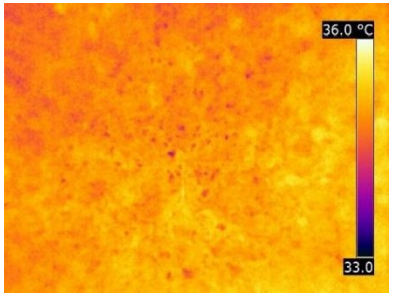	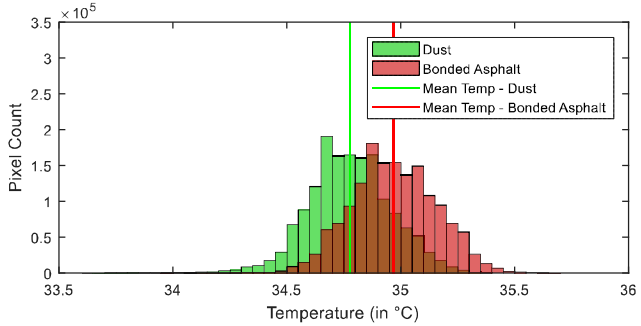
11:30 hours	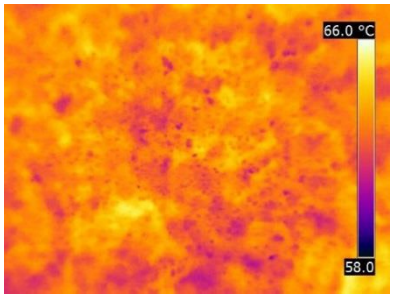	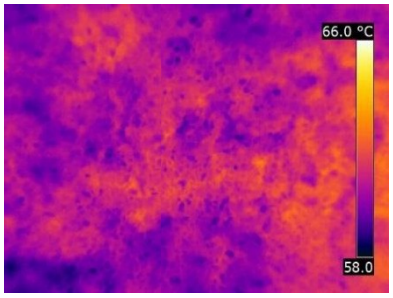	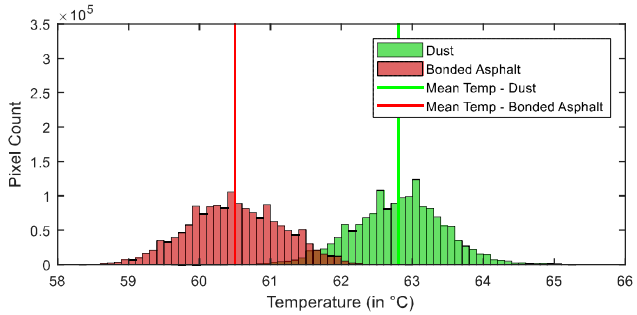

Table 4.5. Infrared images and histograms at different times of the day for grease debonded and bonded asphalt blocks

Time	Raw infrared image		Histogram
02:30 hours	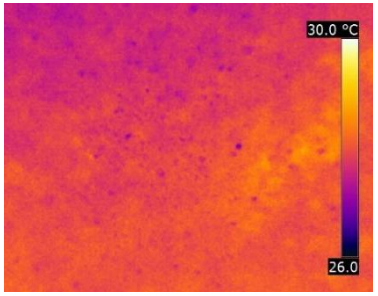	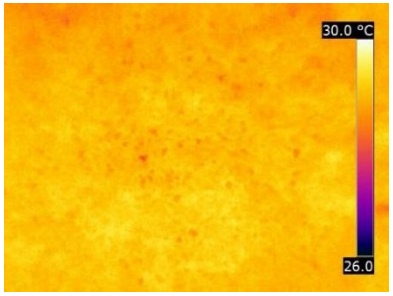	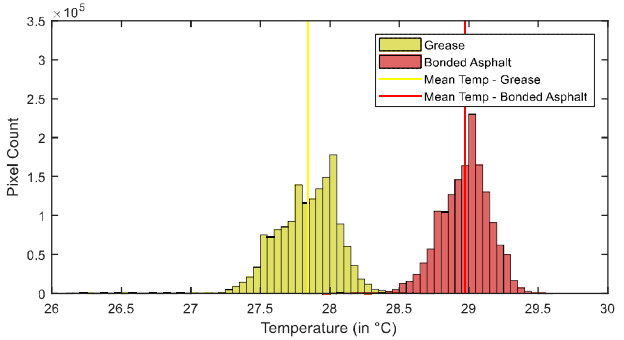
10:00 hours	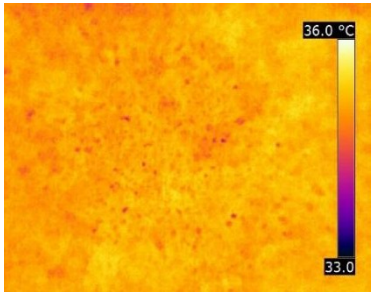	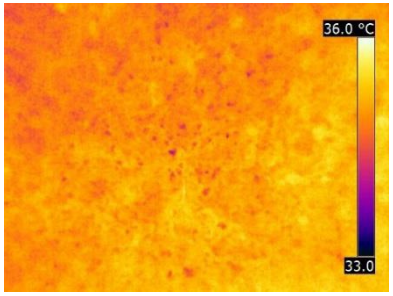	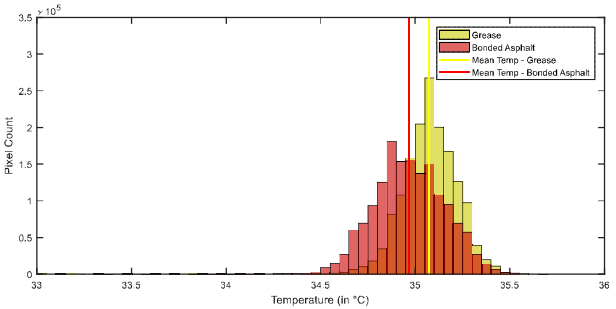
11:30 hours	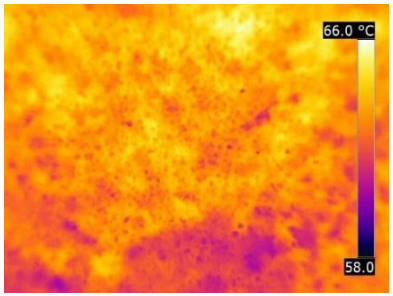	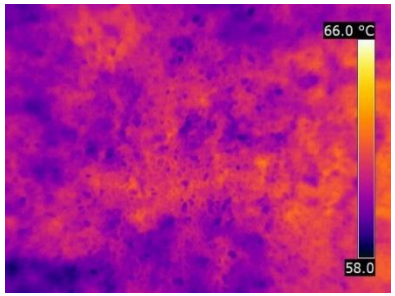	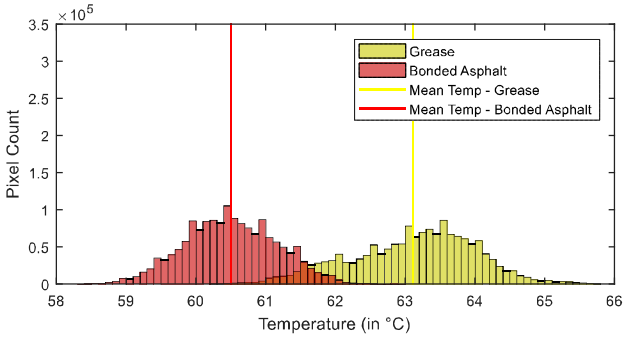

Table 4.6. Infrared images and histograms at different times of the day for polythene debonded and bonded asphalt blocks

Time	Raw infrared image		Histogram
02:30 hours	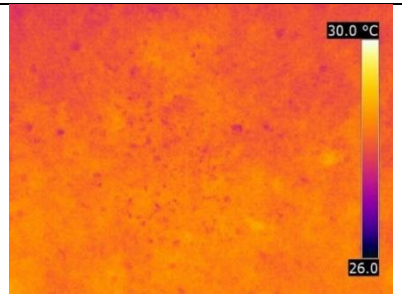	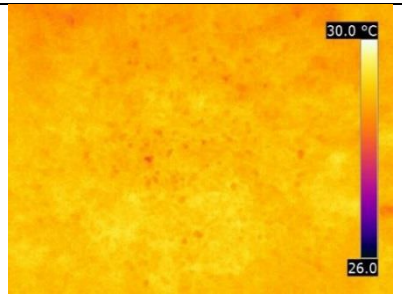	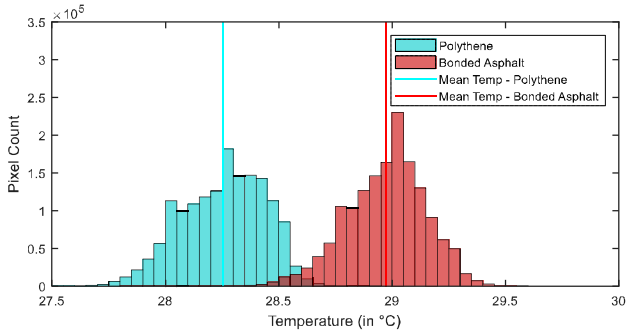
10:00 hours	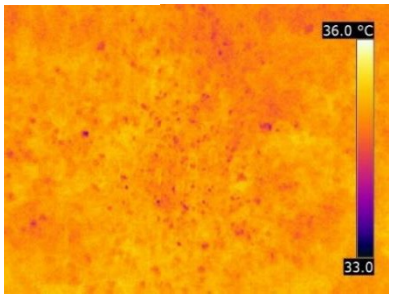	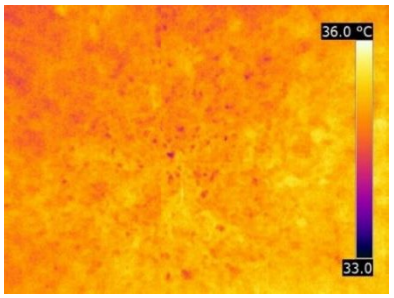	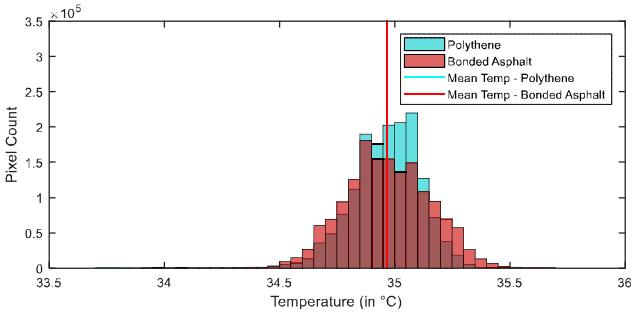
11:30 hours	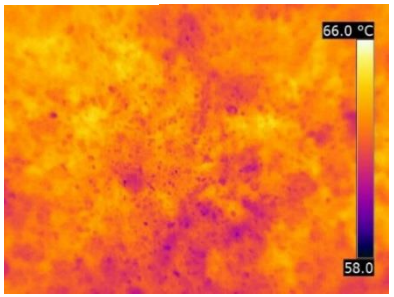	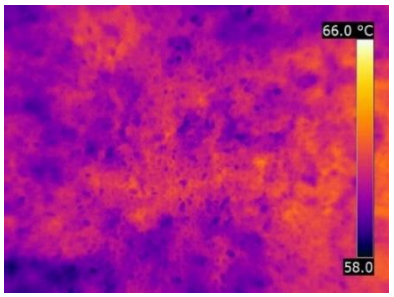	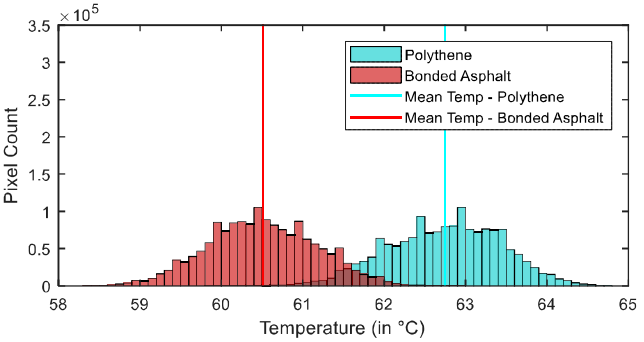

Table 4.7. Infrared images and histograms at different times of the day for bentonite slurry debonded and bonded asphalt blocks

Time	Raw infrared image		Histogram
04:00 hours	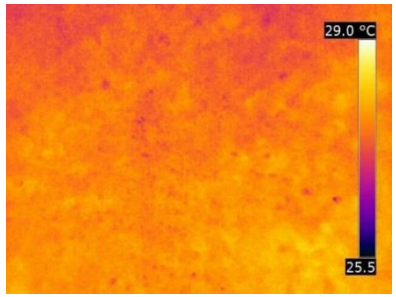	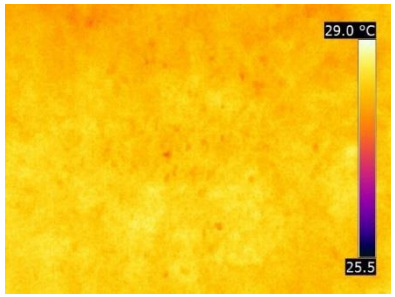	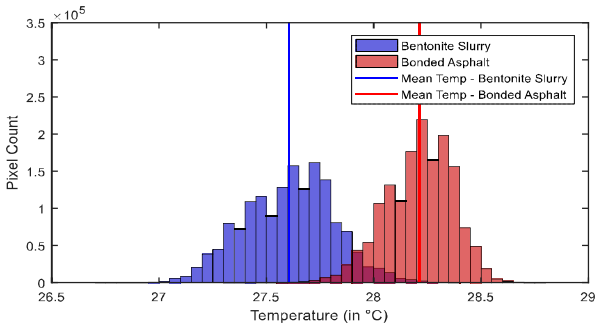
10:00 hours	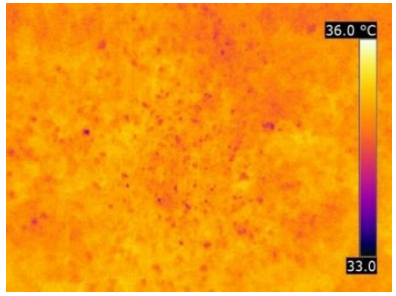	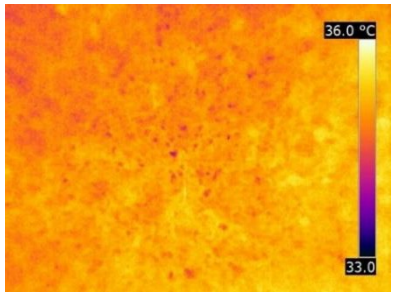	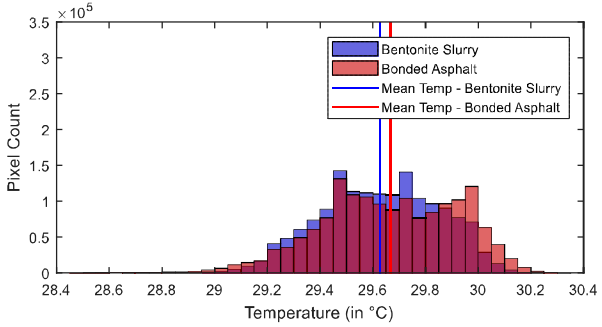
11:30 hours	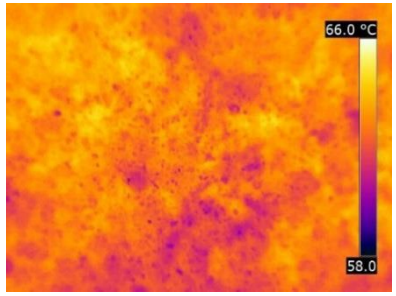	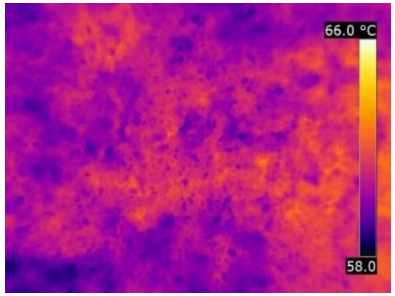	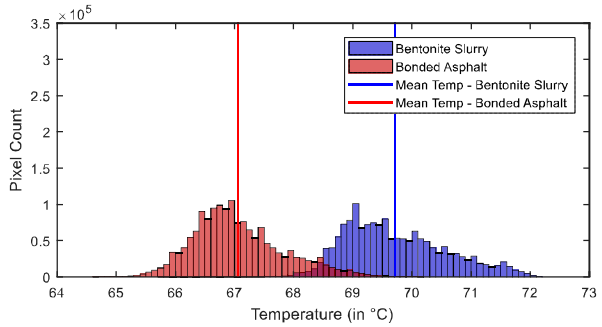

4.3. Evaluation of asphalt pavement test section using GPR method

GPR is a tool used for 2D as well as three-dimensional (3D) imaging of subsurface profiles for effectively mapping the underground features. It can be successfully used to detect metallic as well as non-metallic anomalies. The success of underground flaw or anomaly detection depends on the electrical properties of the host and target materials. The primary applications of GPR were for measuring layer thickness of pavements, and defect detection in bridge deck slab. In case of asphalt pavements, few studies report the usage of GPR for detection of stripping (Cao et al., 2007; Hammons et al., 2006; Rmeili & Scullion, 1997; Saarenketo & Scullion, 1994). The potential detection of delamination in HMA layers using GPR may be done by carefully understanding the radar profiles of the reflected pulses. For well-bonded asphalt pavement layers, only the difference in layer properties may cause some change in GPR signal. The occurrence of debonding at the layer interfaces causing damage and possible infiltration of moisture would produce peculiar reflections in the radar profiles which can be potentially detected using GPR. This is because the dielectric contrast between asphalt (dielectric constant = 3.0 to 6.0) and water (dielectric constant = 81.0) is much greater than that between asphalt and air (dielectric constant = 1.0) (Chen & Zhang, 2009). Apart from the difference in the dielectric constant of the materials, the success greatly depends on the GPR antennae type and frequency.

4.3.1. Instrument

To investigate the ability of GPR to detect asphalt pavement debonding and underground anomaly, the experimental study was carried out on the in-situ asphalt pavement test section. The test section, as explained in Chapter 3, consists of artificially created bonding conditions and anomalies. The 150 mm thick pavement section was radiated by StructureScan Mini containing 1.6 GHz antennae provided by GSSI and shown in Figure 4.15. The instrument was procured with the help of Aimil Ltd., New Delhi.

The 1.6 GHz antenna represent high-resolution, shallow penetration and ground-coupled antenna type. The best performance is achieved by keeping the antenna within 1/10 of the wavelength from the surface and large air gap must be avoided to prevent reflection of radar energy in the air. The radar energy moves perpendicular to the surface of the test medium. The transmitter-receiver offset

in the 1.6 GHz antenna is 58 mm. This indicates that the targets in the top 58 mm may appear fuzzy in raw data which are then corrected using the Background Removal technique.

Figure 4.15. StructureScan Mini

4.3.2. Data acquisition and processing

The instrument was first calibrated by using Auto-Calibration feature by holding it upside down at about 1 m distance from any surface. High scan density of 8 scans/cm was selected. The depth was set as 30 cm. The approximate dielectric of asphalt was set as 6. A series of parallel survey lines spaced at 10 cm longitudinally and 30 cm laterally were marked on the test section, and then the test was carried out by carefully maintaining the alignment of the device. Data were collected at speed ranging from 0.5 to 1 m/s, first along the longitudinal direction and then in the lateral direction resulting in full coverage of the test section.

The data collected with the StructureScan Mini was viewed, processed and documented in commercial software RADAN. Since the anomalies were not located very deep, the quality of obtained GPR data was good, and advanced image processing methods were not required. A few basic processing steps were undertaken which are discussed as under.

4.3.2.1. Time zero

Time Zero Correction is applied to ensure zero time at zero depth from the ground surface by vertically adjusting the position of the entire profile. This correction facilitates correct arrival times, and more accurate depth estimation of target by setting the top of the scan and ground surface level at a close approximation. The time difference occurs primarily due to the presence of

air space between the antenna and surface of inspection, which gets included in the profiles causing inaccuracy in the measurements. 'Automatic' position correction method of time zero is applied, which sets the position of the first positive peak of the direct wave.

4.3.2.2. Background removal horizontal filter

To remove horizontal bands of noise that may be caused by horizontal reflectors or low-frequency noises produced by antenna ringing, background removal technique is used. The application of this filter has to be carefully done to avoid filtering out of any continuous feature within the data.

4.3.2.3. Range gain

During the data collection, if the data is under or over gained, range gain is used to change the gain curve. 'Automatic' gain type is applied to the data to balance the gains over each scan. It helps to amplify the low amplitude signal, thereby enhancing the probability of detection of small features.

The profiles processed after the application of these processing techniques were used to generate 3D depth slices and the 3D views were formed. The profiles and depth slices were thoroughly studied and interpreted to locate the anomalies.

4.3.3. Results and discussion

To map and locate underground anomalies or pavement layer thickness, Linescan display also known as B-scan or radar profile or sectional profile is very useful. The display of data is in the form of colour-amplitude in accordance with the selected colour table and colour transform that assigns a colour to specific positive or negative amplitude value of the recorded GPR signal. The horizontal scale in the profiles, represents the horizontal distance travelled by the radar antenna and it can be changed to the number of scans as well. Similarly, the vertical scale may represent time (in ns) or depth, as per the requirement.

The challenge is to interpret the data and identify the anomalies from the linescans. The objects in linescans appear as hyperbolic reflectors when the radar energy is radiated in a wide beamwidth pattern in order to detect far off objects. Multiple objects often appear as interfering hyperbolic reflectors. The approximate shape, dimension and location of the object are also reflected in the

hyperbolas. For example, the peak of hyperbolic reflections of pipes would be in accordance with its diameter and appear narrower than the hyperbolic reflections of plates that would indicate its approximate width. Similarly, an idea regarding the material of the object or presence of void or debonding can be obtained by observing the brightness of the hyperbolas. For example, the reflections of reinforcement bars (made up of metal) are much brighter than PVC pipes (made up of plastic). Presence of water also produces bright reflections. Various linescans of the test pavement section are presented in the following subsections.

4.3.3.1. Detection of various bonding conditions

Use of GPR in the present study on asphalt pavement test section was not found to be very successful in detecting various bonding conditions induced between the HMA layers. Although in few profiles the pavement layers can be seen with a discontinuity that can be concluded to as debonding but its clear identification could not be established, at other expected locations. Use of other NDT techniques that are capable of giving precise estimates of delamination such as Spectral Analysis of Surface Waves (SASW) method may be helpful in such cases to ascertain its presence. However, due to non-availability of the equipment, SASW tests could not be conducted in the present study.

Figure 4.16 shows the pavement layers at 50 mm, 100 mm and 150 mm depth. The reflections at the depth of 50 mm are unclear and inconsistent. This is an approximate indication of debonding but coring or application of any other NDT method is required to verify this fact in real field conditions.

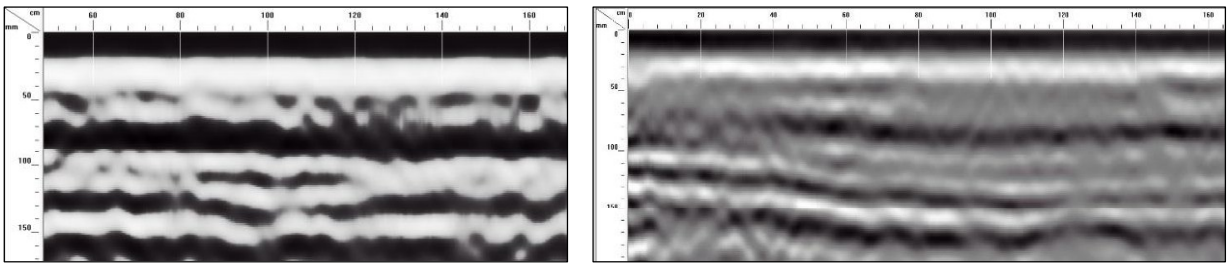

(a) **(b)**

Figure 4.16. Asphalt layers at 50 mm, 100 mm, and 150 mm depth in sectional profile

Figure 4.17 again shows the inconsistency in pavement layers at 100 mm depth, indicative of debonding.

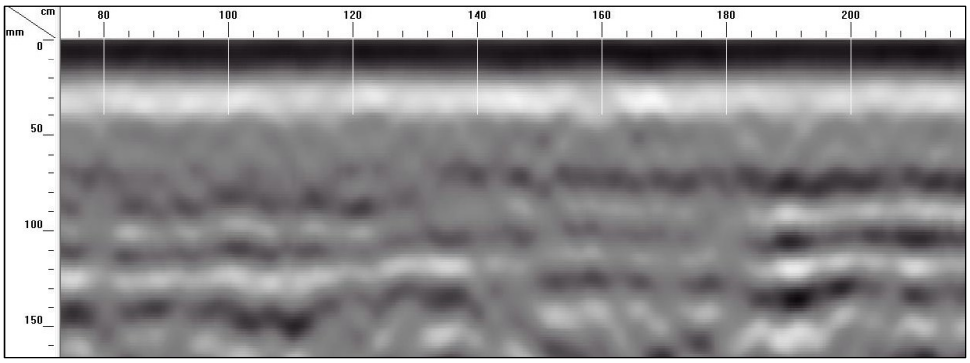

Figure 4.17. Sectional profile showing debonding in asphalt layers at 100 mm

4.3.3.2. Detection of underground anomalies

GPR has been proven to be quite effective in subsurface imaging, as postulated. It has successfully helped in the identification of underground anomalies, along with revealing their approximate shape, dimensions, and depth of placement. Therefore, applications of GPR in asphalt pavements can be extended from measuring pavement layer thickness to anomaly detection as well. However, for interpretation of results, its technical cognizance is mandatory. The following sections discuss the results obtained and their interpretation.

a) Anomalies located along row-1

The anomalies located along row-1 of test section included three PVC pipes (P-1a, P-1b, P-1c) and an L-section of cast-iron (CL) (refer Figure 3.2). Figure 4.18 shows the reflections of three PVC pipes placed at approximate depths of 150 mm, 250 mm and 200 mm, respectively. These were placed before the construction of the test section, by taking out cores at different depths of the existing pavement. The reflections of pipes are not very bright and the identification requires experience. Figure 4.19 shows reflection of CL placed at 50 mm depth. The difference in reflection intensity of pipe and plate is apparent.

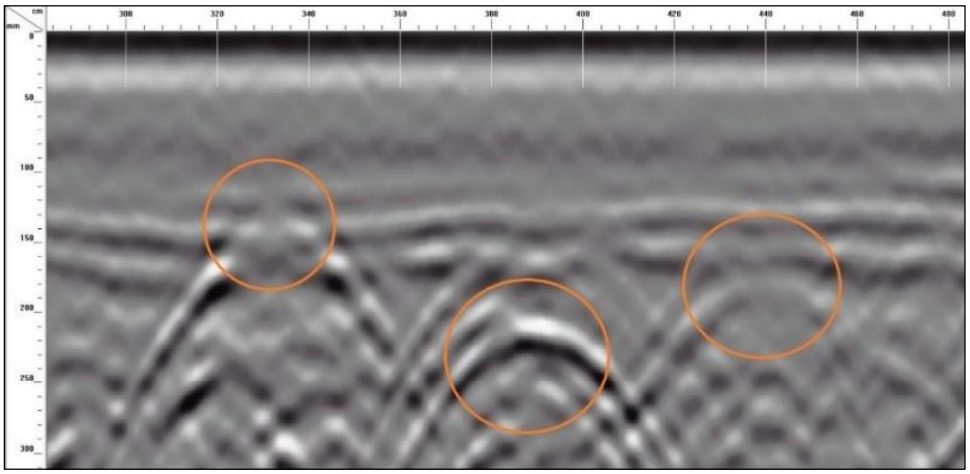

Figure 4.18. Sectional profile showing reflections of PVC pipes buried under the existing pavement

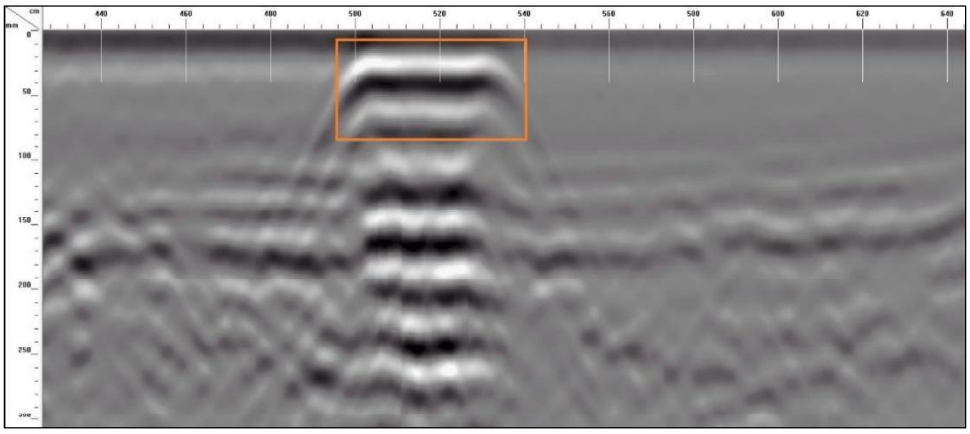

Figure 4.19. Sectional profile showing reflection of CL

b) Anomalies located along row-2

The anomalies located along row-2 of test section included an aluminum plate (A-2), a PVC pipe (P-2), a cast-iron pipe (CI-2), a steel pipe (SP-2) and a wood block (W-2) (refer Figure 3.2). Figure 4.20 shows the reflection of the A-2 in the sectional profile at the expected depth of 100 cm.

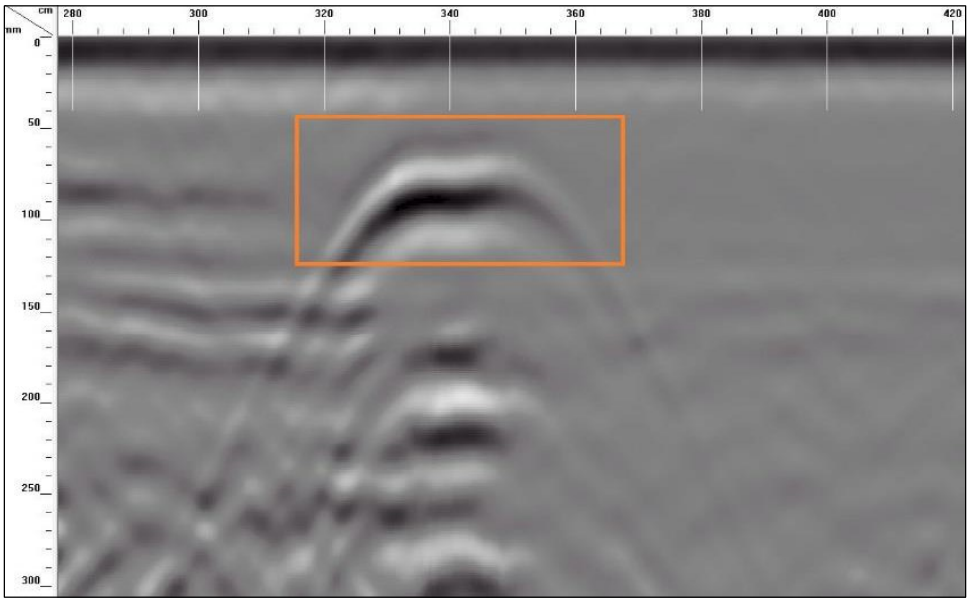

Figure 4.20. Sectional profile showing reflection of A-2

In Figure 4.21 the reflections of cast-iron pipe and steel pipe are shown by square and circle, respectively. The difference in diameters of both the pipes causes difference in the depth of their reflections in the profile. The reflection of the PVC pipe cannot be seen. It is expected to be obscured due to the bright reflection of cast-iron pipe.

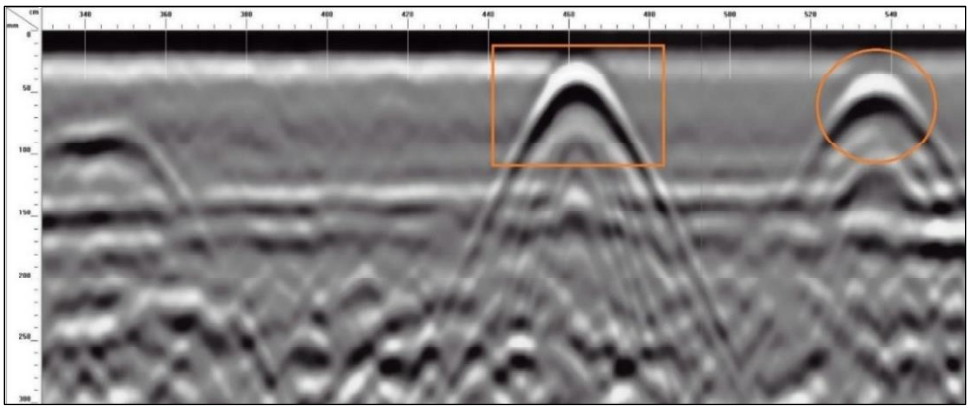

Figure 4.21. Sectional profile showing reflection of CI-2 and SP-2

Figure 4.22 shows the reflection of the wood block (encircled). It can be easily noticed that the reflection of wood is dimmer than the reflection from metals. Also, since the thickness of wood block is less than the diameter of nearby steel pipe, the peak of its reflection appears deeper as compared to the reflection peak of steel pipe in the profile.

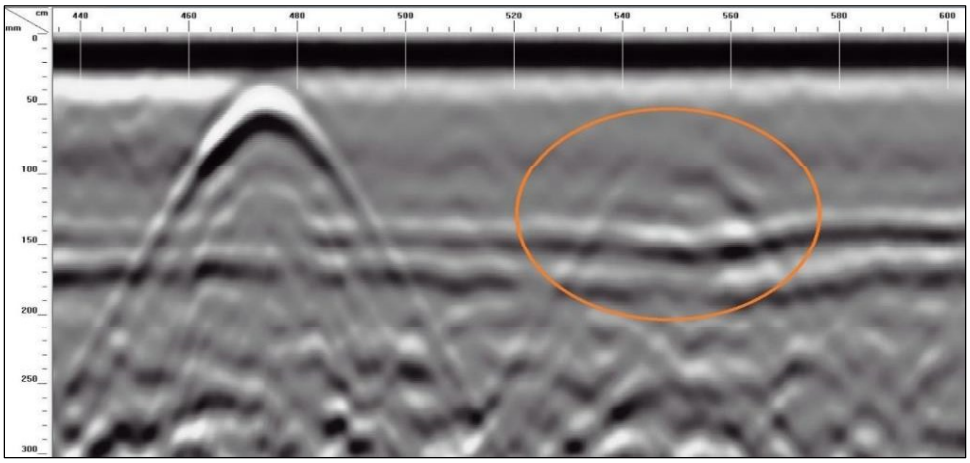

Figure 4.22. Sectional profile showing reflection of W-2

c) Anomalies located along row-3

The anomalies located along row-3 of the test section included an aluminum plate (A-3), a PVC pipe (P-3), a cast-iron pipe (CI-3), a steel pipe (SP-3), a wood block (W-3) and a cast-iron plate (C) (refer Figure 3.2). Figure 4.23 shows aluminum plate in the profile. The shape of the reflection from plate is seen to be flat as compared to hyperbolic reflection from pipes. The approximate size (15 cm) of plate can be noted form the profile. The approximate distance of 60 cm between the objects can also be read from the linescan.

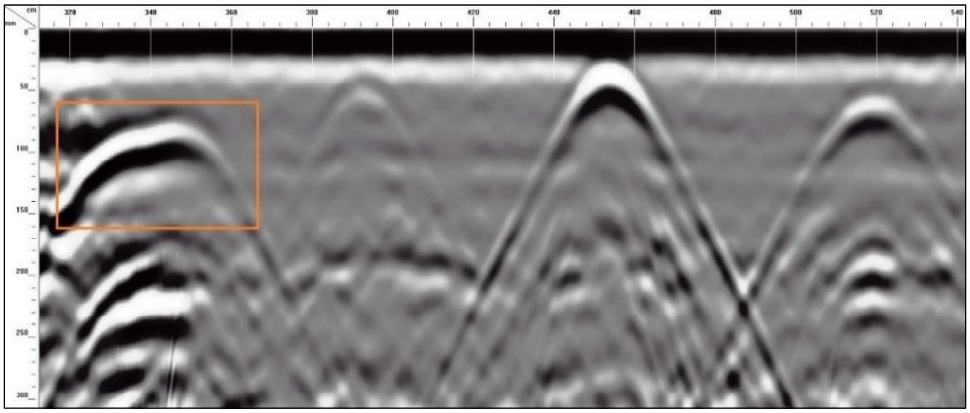

Figure 4.23. Sectional profile showing reflection of A-3

In Figure 4.24 circle shows the cast-iron pipe and square shows the steel pipe. Both being made up of metal, have bright reflections. The difference in their depth is due to the different diameter of both the pipes.

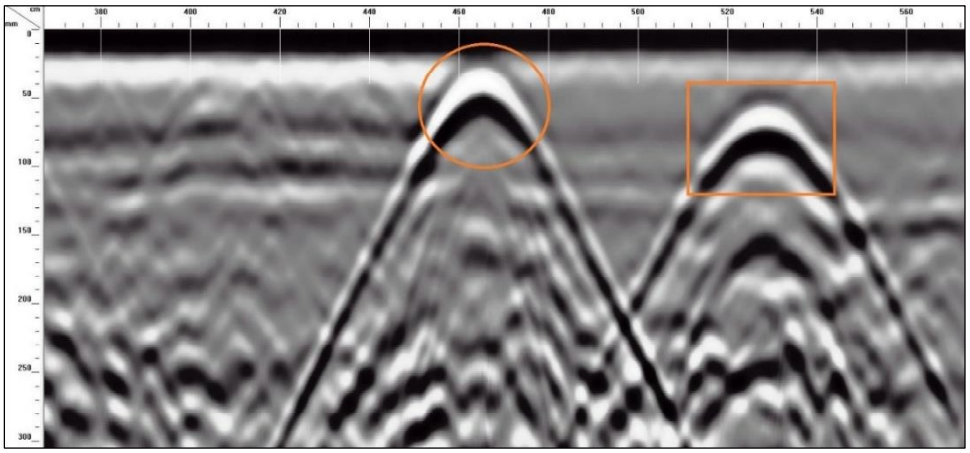

Figure 4.24. Sectional profile showing reflection of CI-3 and SP-3

In the same linescan, Figure 4.25 shows PVC pipe. It can be seen that it is dimmer than the reflection of aluminum plate, cast-iron pipe and steel pipe. In addition to this, the first dominant colour is black instead of white, which indicates a reflection that begins with a negative and not positive polarity.

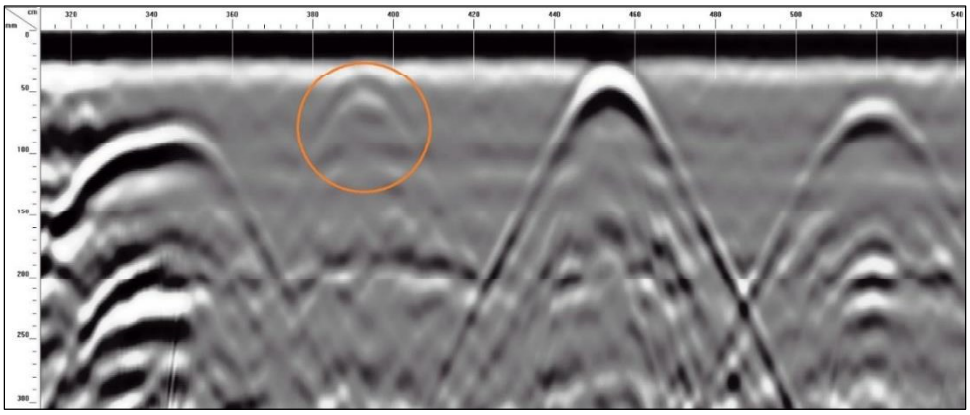

Figure 4.25. Sectional profile showing reflection of PVC-3

Figure 4.26 shows the cast-iron plate with bright and flat reflection. The 40 cm size of plate can be read at its close approximation.

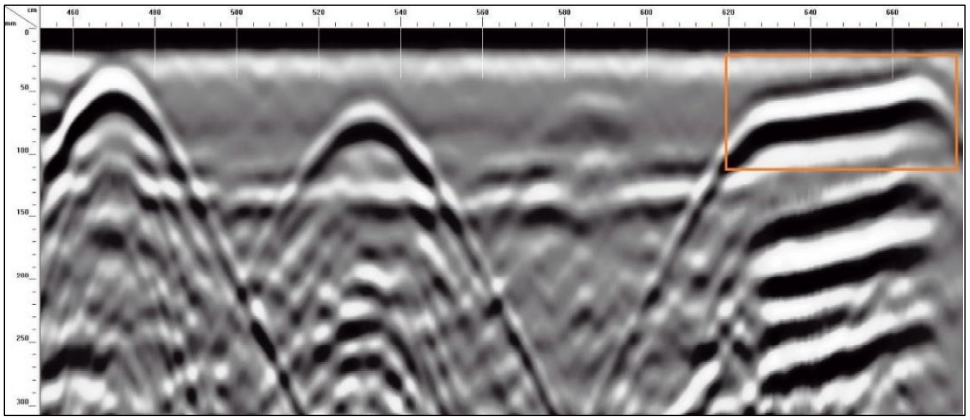

Figure 4.26. Sectional profile showing reflection of C

It may be noted that the position of the objects are slightly displaced from their initial position due to the disturbances during construction activities. The objects, particularly placed along row-3 and directly over the existing pavement section were expected to be at the depth of 150 mm. However, during the compaction of the overlay by the roller, this particular part of the test section got slightly more compacted which reduced its thickness. Therefore, the reflections of the objects in the linescan appear at shallower depths. Figure 4.27 shows the wood block reflection in the profile.

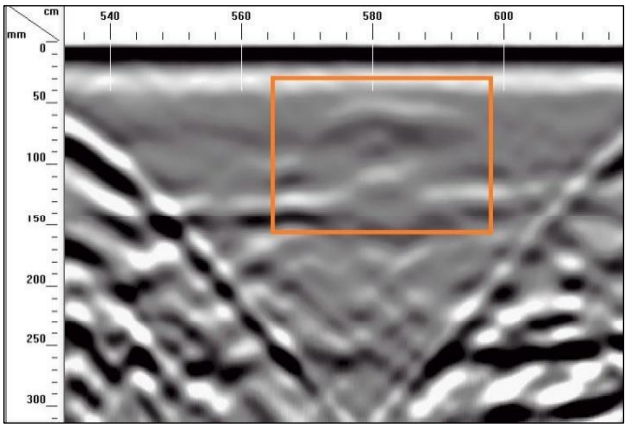

Figure 4.27. Sectional profile showing reflection of W-3

4.3.3.3. 3D depth slice

The 3D view of the entire asphalt pavement test section is created using RADAN software. Figure 4.28 shows the subsurface view at the surface and various depth slices of 5 cm, 10 cm, 15 cm and 20 cm. It can be seen that the anomalies are faintly visible at the surface and 20 cm depth but

strongly visible at 10 cm deep slice due to their actual placement at this depth. The various anomalies can be seen in red colour.

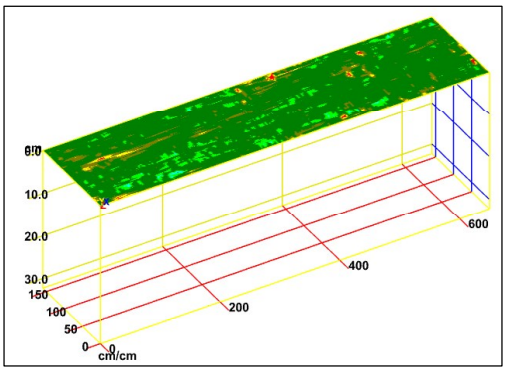

(a) At surface

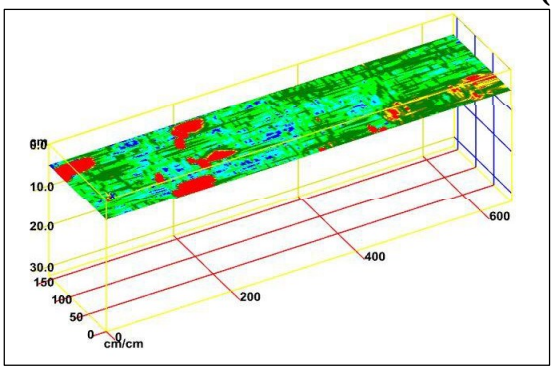

(b) 5 cm depth

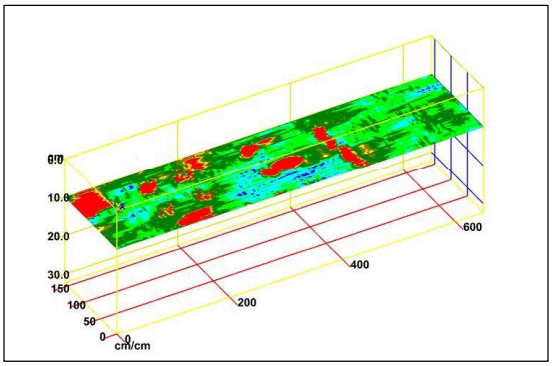

(c) 10 cm depth

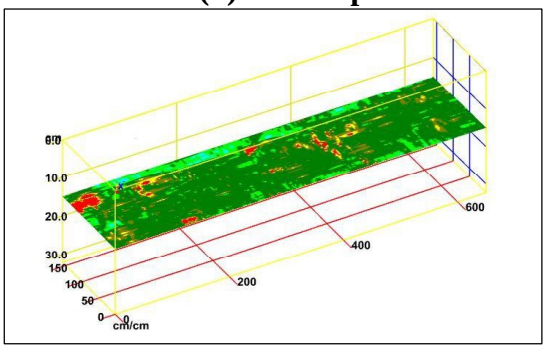

(d) 15 cm depth

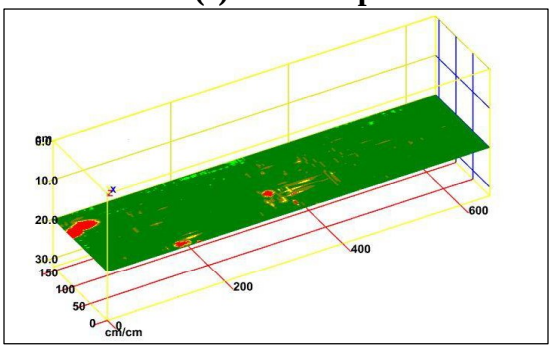

(e) 20 cm depth

Figure 4.28. Depth slices of GPR data at various depths

Developing a 3D field of vision enabled the reflections of underground anomalies to be viewed at their actual locations and facilitated better presentation with enhanced understanding. Appendix-2 complies these 3D results along with their sectional profile to gain better insight.

4.4. Evaluation of asphalt pavement test section using LWD method

LWD is primarily used for strength evaluation of subbase layers and subgrade soils. This work makes an attempt to explore its suitability for debonding detection on asphalt pavements. Although literature reports very less success for debonding and anomaly detection using LWD, still it was used in this study because of the equipment availability, simplicity to operate, and it added no cost to the research.

4.4.1. Instrument

Light weight deflectometer (Figure 4.29) is a portable structural testing equipment. Load application is impulse transient type and response in the form of deflection is measured at the radial points with the help of sensors. Dynatest 3031 LWD (3031-1081 version 1.0.3) is used in this study which meets the ASTM E2583-07 standard (ASTM E2583-07, 2015).

Dynatest LWD uses a drop weight of 10 kg, 15 kg or 20 kg and loading plate of diameter 150 mm or 300 mm can be selected. It measures the load using a load cell, in range of 0 to 25 kN. The weight is dropped onto a rubber buffer located on the top of load cell. One to three sensors known as geophones of measurement range from 0 to 2200 μm can be used. Precision of each geophone is 0.1 μm and it works on sampling frequency of 4000 Hz. Height of drop is adjustable with maximum up to 850 mm. Time-history plots of the measurements from the load cell and the geophones are recorded and presented.

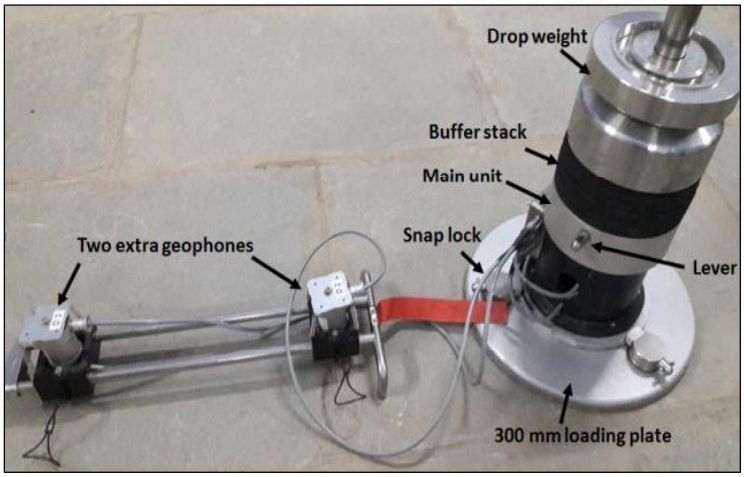

Figure 4.29. Dynatest LWD

4.4.2. Data acquisition

The drop weights used for LWD testing on the asphalt pavement test section were 10 kg, 15 kg and 20 kg. Three geophones (D1, D2 and D3) were used in this study with configuration as 0 (D1), 300 mm (D2) and 600 mm (D3) from the center of load cell. Loading plate of 150 mm diameter was used. Not much information was provided by D3 geophone and the deflections measured by it were close to zero. Three rounds of testing, each for three drop weights were conducted on different debonded and bonded blocks to compare the measured deflections of a fully bonded area to a debonded area. Theoretically, a debonded section should have higher deflection than a section that is fully bonded. However, the fully bonded block provided similar deflection measurements to those blocks with debonding. The probable reason could be low magnitude of load used in LWD (maximum 20 kg), which would be insufficient to produce deflection in pavements. On the basis of these results, the use of LWD was found to be insignificant and it was not used further in this study. Figure 4.30 presents a typical time-history plot of applied load and measured deflection (geophone D1) obtained during LWD testing of the test section.

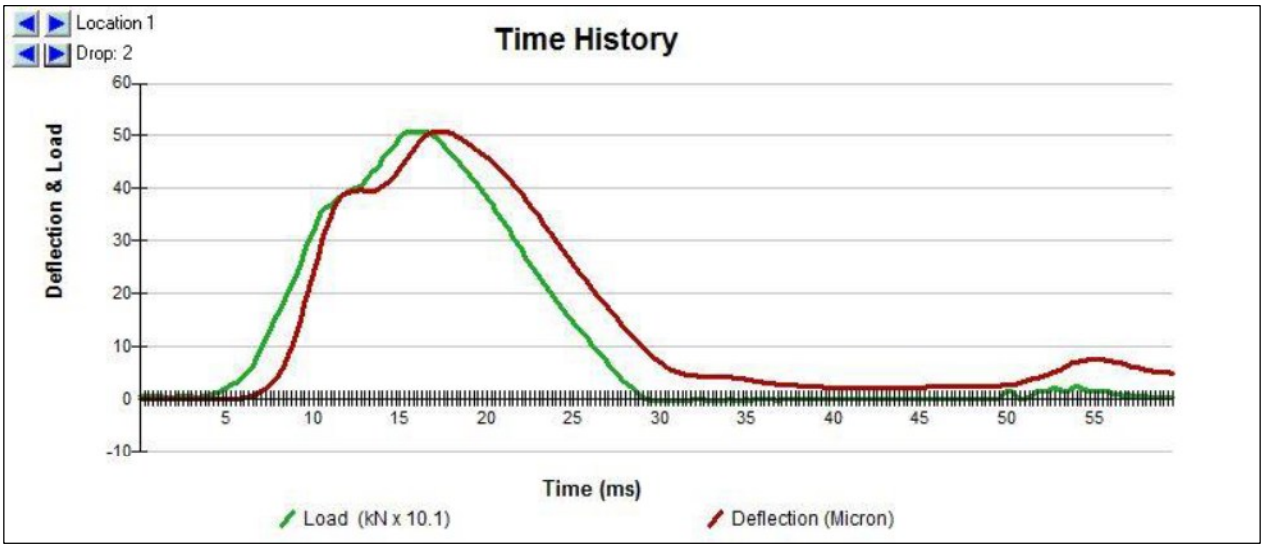

Figure 4.30. Time-history plot of LWD data

4.5. Concluding remarks

This study is performed by using three NDT techniques to detect delamination between HMA layers and identify underground anomalies under in-situ asphalt pavement test section constructed with simulated defects. The techniques include IRT, GPR and LWD. Each one of these NDT techniques is found to have its own advantages and limitations. The summary of their performance is presented in Table 4.8.

Table 4.8. Performance summary of NDT technologies on asphalt pavement test section

Factors	**IRT**	**GPR**	**LWD**
Detection of delamination	Good (shallow)	Fair	Poor
Detection of underground anomalies	Poor	Good	Poor
Equipment availability	Available	Limited	Available
Application in India	Limited use	Limited use	Used on soil
Cost in India	Fair	High	Fair
Data collection	Area-based	Area-based	Point-based
Effective depth	Fair	Good	Good
Ease of data analysis	Fair	Poor	Fair
Results	2D map	2D map	Point list
Advantages	Quick area coverage	Quick 3D subsurface condition information collection	Low cost
Limitations	Effective for shallow depths	High cost; complex data analysis	Point load testing; poor performance on pavements due to less load

IRT is concluded to be highly successful for detecting shallow delamination (upto 50 mm in this study). It should be preferred for field inspections since it is capable of quickly scanning large areas and results in saving labour costs and time in data collection. The novel methodology proposed in this work excellently facilitates in deriving the field inspection time of asphalt

pavements using IRT. Night-time is concluded to be optimum for thermographic inspections due to the absence of interchange time zones during night hours. The limitations include the inability to provide information about the depth of flaw and difficulty to detect deep debonding. IRT also performed poorly to detect underground anomalies. The possible reason may be the inhomogeneity of asphalt mix and small size of anomalies that could not generate sufficient thermal contrast to be detected by thermal camera. Use of higher resolution infrared cameras may help to overcome these limitations which were not available for the present study. Also, in the case of the passive approach of IRT, the results are considerably affected by environmental conditions such as cloud cover and wind, since they affect the heating of pavement.

GPR has shown excellent ability in locating and imaging subsurface anomalies but showed poor performance in detecting air-filled debonding. Only, few traces of discontinuity in reflections of pavement layer were identified at some locations in sectional profiles that were indicative of delamination. However, precise conclusions could not be obtained. Hence, combination of GPR with IRT could not help to derive more information about debonded areas. Moisture-infiltrated debonded areas have fairly higher chances of detection using GPR, as reported in literature (Heitzman et al., 2013). Due to time constraints, GPR tests over moisture-infiltrated debonding could not be performed in this study. GPR is reported to identify electromagnetic properties and not mechanical properties. Its performance greatly depends on the choice of suitable antenna type according to the depth of the target to be located, and should be selected accordingly. LWD could neither perform well for delamination detection nor for locating underground anomalies. Higher load variant of LWD, namely Falling Weight Deflectometer (FWD) may provide some significant results for detection of delamination. Additionally, none of the technologies could identify the debonding due to inadequate application of tack coat.

Owing to the unavailability of better-quality infrared cameras, FWD and difficulty in procuring other NDT tools such as mechanical wave-based methods, these tests could not be conducted in this study. Further, the outcome of the proposed methodology can be enhanced by performing tests at pavements with unknown bond conditions so that analysis can capture the uncertainty of the location of the debonded area associated with exact extent of real defects. The next chapter

discusses the application of the NDT technologies on concrete bridge decks for detecting commonly occurring internal flaws in bridge decks.

Although the application of NDT technologies has numerous advantages with the availability of software to analyze the data yet the data analysis requires a highly trained technician to understand the relation between pavement condition and obtained signals that consumes considerable time. Improvement in the level of data analysis automation is required to make the entire process more efficient. In spite of the fact that these technologies effectively identify a change, or discontinuity, in the pavement condition but they fail to determine the reason of this change. To confirm the characteristics of discontinuity, coring is still required a few times at critical locations.